ACS OMEGA

Open Access

http://pubs.acs.org/journal/acsodf

Article

Use of Mesenchymal Stem Cell-Targeting 3WJ Nanoparticles and Reported Specific Delivery of Anti-miRNA 138 to Treat Osteoporosis

Liangliang Xu,[⊥] Xiangzhong Liu,[⊥] Jian Chen,[⊥] Liwei Xu, Aofei Yang, and Zhanghua Li*

Cite This: *ACS Omega* 2025, 10, 10633−10641

Read Online

ACCESS | Metrics & More | Article Recommendations

ABSTRACT: Purpose: Locked nucleic acid (LNA)-modified anti-microRNAs have been demonstrated to target mesenchymal stem cells (MSCs) to treat bone diseases. However, the "off-target" effect limits its clinical application. Methods: We selected specific aptamer M4 of MSCs and employed the three-way junction (3WJ) as the core scaffold to construct nanoparticles (3WJ-M4-LNA) for specific delivery of anti-miRNA 138. Results: Our results suggested that the 3WJ-M4-LNA nanoparticles, not 3WJ-M4 or 3WJ-LNA, can specifically deliver anti-miRNA to MSCs, resulting in significant inhibition of miRNA 138 expression. Our experiment further confirmed that the nanoparticles can promote MSCs' osteogenic differentiation by activating the ERK1/2 pathway. In vivo, the nanoparticles promoted bone formation and improved the bone microarchitecture in rabbit osteoporosis models. Conclusions: These results indicate that the 3WJ nanoparticles could develop as a specific therapeutic strategy for osteoporosis.

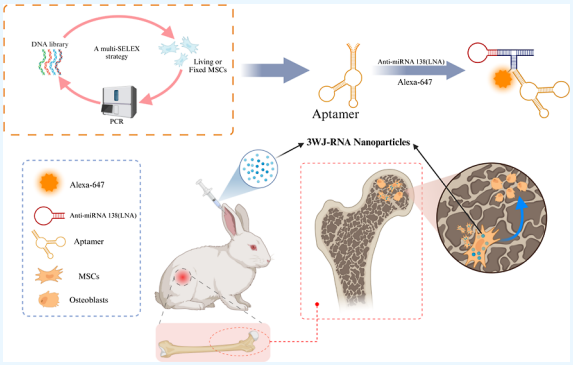

INTRODUCTION

As a metabolic skeletal disease, osteoporosis (OP) is characterized by low bone mass, low bone mineral density, and high fracture risks and poses major clinical challenges.[1,2] Mesenchymal stem cells (MSCs) have been widely studied for treating bone diseases because of their osteogenic functions.[3−5] As noncoding RNAs, microRNAs (miRNAs) can negatively regulate translation of their target mRNAs through RNA interference after binding to complementary sequences in their target mRNAs.[6−8] Recently, miRNA-based methods have shown great potential for treating bone diseases.[9] For example, miRNA 138 have been confirmed to be a negative regulator of osteogenic differentiation of MSCs and can inhibit bone formation.[10,11] This means that anti-miRNA 138 can serve as a therapeutic agent to treat OP. However, a major problem for translating miRNA-based methods into clinical applications is the lack of MSC-specific osteogenic miRNA delivery systems.

Aptamers are single-stranded nucleic acids that can be generated by an iterative process termed systematic evolution of ligands by exponential enrichment (SELEX) technology from randomly synthesized DNA or RNA libraries.[12−14] They can fold into special spatial structures or three-dimensional (3D) architectures and connect to targets with great affinity and specificity.[15,16] Compared with traditional antibodies, aptamers have unique benefits owing to their ease of synthesis, consistency, facile chemical modification, low immunogenicity and toxicity, and strong chemical stability. These advantages provide aptamers with broad application prospects in the fields of therapeutics, drug delivery, and biosensing.[17−19]

In this study, we developed MSC-delivery RNA nanoparticles for anti-miRNA 138. The nanoparticles can be constructed by bottom-up self-assembly of the three-way-junction (3WJ) derived from the bacteriophage phi29 packaging RNA (pRNA).[20−22] The 3WJ motif can carry different functional modules with excellent serum stability and biosafety and has been explored as a core scaffold for delivering different therapeutic agents (siRNA, miRNA, and other drugs) to target cells.[23−29] First, a multistrategy SELEX was designed to select MSC-specific aptamers. By the multistrategy SELEX, aptamer M4 was obtained. Then, the 3WJ motif was used to connect M4 and anti-miRNA 138 for MSC-specific recognition and intervening. Finally, aided with the specificity of M4, this delivery system achieved MSC-specific delivery of anti-miRNA 138 and facilitated bone formation.

MATERIALS AND METHODS

Cell Culture. MSCs[30] were isolated and cultured according to previous methods. In brief, MSCs were obtained from whole bone marrow through an adherent method and cultured through marrow mesenchymal stem medium (MSCM,

Received: December 22, 2024
Revised: February 20, 2025
Accepted: February 25, 2025
Published: March 4, 2025

Cyagen, USA). Then, the chondrogenic differentiation ability of MSCs was detected with chondrogenic differentiation medium (Cyagen, USA) for 3 weeks. For surface marker characteristics, after being collected and washed, MSCs were incubated with primary antibodies anti-CD29 (Bioss, bs-0486R, 1:500), anti-CD44 (Bioss, bs-2507R, 1:500), and anti-CD45 (Bioss, bs-0522R, 1:500) for 30 min at 4 °C. After being washed, MSCs were incubated with FITC-conjugated secondary antibody (Bioss, bs-0295G, 1:2000) for 30 min at 4 °C and analyzed by a flow cytometer (Beckman, USA).

Rabbit peripheral blood mononuclear cells (PBMCs) and kidney cells were the preservative cells in our laboratory.

Random Library and Primers. The synthetic ssDNA library (termed GP40) consisted of a random sequence of 40 nucleotides: (5′ -GCAATGGTACGGTACTTCC-N40-CAAAAGTGCACGCTACTTTGCTAA-3′). A forward Plong-1 primer (5′ -GCAATGGTACGGTACTTCC-3′) and a reverse P11 primer (5′ -TTAGCAAAGTAGCGTG-CACTTTTG-3′) were used to synthesize double-stranded DNA (dsDNA) via a standard PCR procedure. The primer Plong-1 and Pstemloop-3 primer (5′-GCTAAGCGGGTGG-GACTTCCTAGTCCCACCCGCTTAGCAAAGTAGCGTG-CACTTTTG-3′) were used to synthesize single-stranded DNA (ssDNA) by unequal length strand PCR. The random library and primers as well as the aptamers were synthesized by Sangon Biotech Co., Ltd. (Shanghai, China).

Cell-SELEX. We constructed a multistrategy SELEX to select aptamers. Suspension selection of fixed cells (the first strategy), suspension selection of living cells (the second strategy), and adhesion selection of living cells (the third strategy). For the first strategy, 1×10^6 fixed P3MSCs were incubated with the denatured ssDNA library at 4 °C for 40 min in screening buffer I [1 × phosphate buffered saline (PBS), 5 mM $MgCl_2$, 0.1 $\mu g/\mu L$ ytRNA, and 1% BSA]. For the second strategy, 1×10^6 living P3MSCs were incubated with the denatured ssDNA library at 4 °C for 40 min in screening buffer I. For the third strategy, 1×10^6 adherent P3MSCs were incubated with the denatured ssDNA library at 37 °C for 40 min in screening buffer II (1 × PBS, 100 mM NaCl, 2 mM $MgCl_2$, 1 mM $CaCl_2$, 0.1 $\mu g/\mu L$ ytRNA, and 1% BSA). After removal of the unbound oligonucleotides, the bound oligonucleotides were amplified via unequal length PCR and purified as the next round of library. From the fourth round, negative selection was introduced. After multiple rounds of selection, a flow cytometer was used to detect the enriched DNA pools. Then, the enriched DNA pool from the first strategy was detected using monoclonal sequencing by Sangon, Shanghai, China. While the enriched DNA pools from the other two strategies were sequenced via high-throughput sequencing by the Institute of Hydrobiology, Chinese Academy of Sciences, Wuhan, China.

Design and Synthesis of 3WJ-M4-LNA Nanoparticles. 3WJ-M4-LNA nanoparticles were designed and constructed according to the bottom-up approach.[31] The 3WJ core was used as the scaffold, the M4 aptamer as the targeting ligand, locked nucleic acid (LNA)-modified anti-miRNA138 as the therapeutic agent, and Alexa 647 as the imaging module. All of the strand sequences are described below. Lowercase letters indicate 2′-F modified nucleotides:

The core sequences of pRNA-3WJ:

A_{3WJ}: 5′-uuGccAuGuGuAuGuGGG-3′

B_{3WJ}: 5′-cccAcAuAcuuuGuuGAucc-3′

C_{3WJ}: 5′-GGATCAATCATGGCAA-3′

The therapeutic 3WJ-M4-LNA is composed of four strands:

3WJA: 5′-uuGccAuGuGuAuGuGGGAucccGcGGc-cAuGGcGGccGGGAG-3′ (underlined sequence is extended sequence[48]).

3WJB: 5′- Alexa 647:5′-cccAcAuAcuuuGuuGAucc (Alexa 647)-3′

3WJC: 5′-GCAATGGTACGGTACTTC-CATTGGTCTTCGCGATCAATTCGCTACGCGCGCC-TAGCCTGCAAAAGTGCACGCTACTTTGCTAACCCG-GATCAATCATGGCAA-3′ (underlined sequence is aptamer M4).

Anti-miRNA138 LNA: 5′-AtTcaACAacAc-CaGCCTCCCGGCCGCCATGGCCGCGGGAT-3′ (underlined sequence is anti-miR138 LNA138[10] and ununderlined sequence is extended sequence).

All of these strands were synthesized by Sangon Biotech Co., Ltd. (Shanghai, China).

The four fragments were mixed at equal molar concentrations to assemble nanoparticles in PBS buffer (1 × PBS, pH = 7.4, and 50 mM MgCl2) and heated to 95 °C for 5 min and slowly cooled over about 45 min to 4 °C. Assembly efficiencies of 3WJ nanoparticles were confirmed by 12% native polyacrylamide gels (PAGE) at 100 V for 1 h in TBE running buffer (89 mM Tris, 200 mM borate acid, and 5 mM MgCl2) at 4 °C, Then they were stained with GelRed followed by imaging by the gel imaging system (Bio-Rad, USA).

Serum Stability of Nanoparticles. 500 nM of 3WJ-M4-LNA nanoparticles were incubated in fetal bovine serum (FBS, final concentration is 50%). Samples were taken at multiple time points, including 0, 1, 2, 4, 8, 12, 24, and 36 h after incubation at 37 °C. Then, stained with GelRed followed by electrophoresis with 12% native PAGE gel.

Physical Characteristics Measurement of Nanoparticles. A Zetasizer Nano ZSP (Malvern Instruments, Malvern, UK) was employed to measure the hydrodynamic sizes and zeta potential of 3WJ-M4-LNA nanoparticles by using a detection angle of 173° at a temperature of 25 °C. The Nano ZSP uses a 10 mW He−Ne laser operating at a wavelength of 633 nm.

Flow Cytometry Analysis for MSC Binding of 3WJ Nanoparticles. MSCs were incubated with 3WJ-M4-LNA (100 nM) in 100 μL of PBS solution at 37 °C for 40 min after being collected. Then, MSCs were washed and resuspended in PBS and analyzed by flow cytometry (Beckman, USA).

Confocal Microscopy Imaging Analysis for Endocytosis. MSCs were incubated with 100 nM 3WJ-M4-LNA-Alexa 647 nanoparticles at 37 °C for 2 h. Then, MSCs were washed with PBS and fixed with 4% paraformaldehyde for 30 min. Alexa Fluor 488 phalloidin (Servicebio, China) and DAPI (Servicebio, China) were added to stain the cytoskeleton and nucleus. The cells were then observed by confocal microscopy (Leica, Germany).

Real-Time PCR Analysis. MSCs were incubated with different concentrations of 3WJ-M4-LNA nanoparticles for 48 h. Then, miRNA was extracted using the Trizol RNA extracting solution (TOYOBO, Japan) and reverse-transcribed into cDNA using a cDNA synthesis kit (TOYOBO, Japan).

The relative miRNA expression of miRNA-138 was detected through the SYBR Green Realtime PCR Master mix (TOYOBO, Japan). U6 was used as an internal control. The primer sequences of miRNA-138 and U6 were designed by the manufacturer (RiboBio, China). qPCR was performed by the

https://doi.org/10.1021/acsomega.4c11505
ACS Omega 2025, 10, 10633−10641

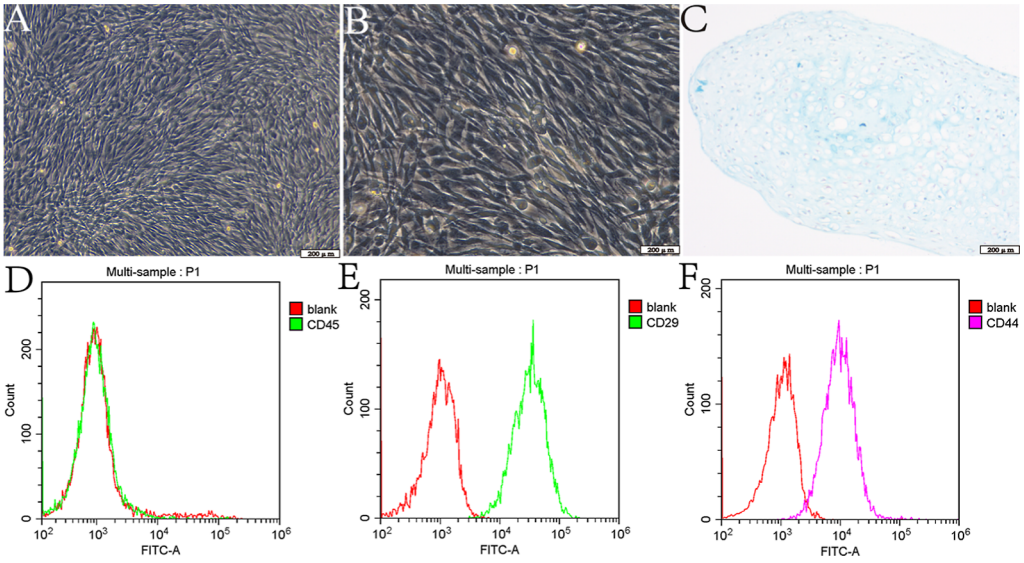

Figure 1. Identification of MSCs. (A−C) MSCs were observed by an inverted microscope (100× and 200×) and identified by Alcian blue staining. (D−F) Flow cytometry was used to detect cell surface markers (CD29, CD44, and CD45).

Bio-Rad CFX Manager system (Bio-Rad, USA), The relative expression of miRNA was calculated by $2^{-\Delta\Delta Ct}$.

Western Blot Analysis. According to the result of qPCR experiment, the optimal concentration of 3WJ-M4-LNA was 200 nM. Then, MSCs were incubated with 200 nM 3WJ-M4-LNA nanoparticles for 48 h. Western blot analysis was used to detect the osteogenesis-related proteins including runt-related transcription factor 2 (Runx2, bs-1134R, Bioss, Beijing, China), osteopontin (OPN, bs23258-R, Bioss, Beijing, China), and glyceraldehyde-3-phosphate dehydrogenase (GAPDH, GB11002, Servicebio, Wuhan, China). Total protein was separated by 10% SDS-PAGE and transferred to a PVDF membrane (Millipore, USA) followed by blocking with 5% skim milk for 2 h. The PVDF membrane was incubated with primary antibodies against Runx2 (1:2500), OPN (1:2000) and GAPDH (1:2500) at 4 °C overnight. Then, they were incubated with secondary antibodies (1:20,000) at room temperature for 1 h. Finally, these protein bands were visualized using enhanced chemiluminescence (G2020, Servicebio, Wuhan, China) and exposed by the gel imaging system (Biorad, USA). ImageJ software analyzed the grayscale and used GAPDH as the internal reference.

Osteogenic Differentiation Staining. To assess the osteogenesis of the 3WJ-M4-LNA nanoparticle-delivery MSCs, MSCs were incubated with 200 nM 3WJ-M4-LNA nanoparticles for 14 days by changing the culture medium and 3WJ-M4-LNA nanoparticles every 3 days. Then, MSCs were washed and fixed with polyformaldehyde. Later, alkaline phosphatase (ALP) and mineralized nodule were displayed via staining with the BCIP/NBT ALP color development kit (Beyotime, China) and alizarin red (Cyagen, USA).

OP Model Establishment and Treatment. 2 month old Japanese white rabbits (body weight 2.5 ± 0.5 kg) were provided by the Animal Facility of the Wuhan wan qian jia xing Biotech Co., Ltd. (Lenience no. SCXK Hubei 2023−0011), without a specific requirement for sex, and raised in a single cage with a normal diet. All of the animal experiments were approved by the Ethics Committee of Wuhan Third Hospital, Tongren Hospital of Wuhan University, and followed the Guide for the Care and Use of Laboratory Animals.

After allowing these rabbits to acclimatize for 1 week, the rabbit model of OP was established according to the previous method.[32] Briefly, these rabbits were divided into four groups (6 rabbits per group): (1) the model group, (2) the 3WJ-M4 group, (3) the 3WJ-LNA group, and (4) the 3WJ-M4-LNA group. All rabbits were administered with retinoic acid (RA) (90 mg/kg in 2 mL 0.9% saline) via gavage for 14 days to develop an OP animal model. Rabbits in the model group, 3WJ-M4 group, 3WJ-LNA group, and 3WJ-M4-LNA group were administered with normal saline, 100 μM 3WJ-M4 in 1 mL PBS, 100 μM 3WJ-LNA in 1 mL PBS, and 100 μM 3WJ-M4-LNA in 1 mL PBS, respectively, through the ear vein at 1 week and 3 weeks after model establishment.

Biodistribution and Toxicity Analyses of Nanoparticles. According to previously method,[33] the rabbits were injected with 3WJ-M4-LNA-Alexa 647 for 12 h, then the rabbits were sacrificed and organs (hearts, livers, spleens, lungs, kidneys, and femurs) were collected. The fluorescence imaging was performed using an IVIS Lumina LT imaging system. What is more, the toxicity reaction of these organs was detected by H&E staining.

Micro CT Imaging. Micro CT (Skyscan1276, Bruker) was taken to detect bone mass and bone microarchitecture in the femur. The scanning parameters are as follows: the filter is Al + Cu and the resolution ratio is 20 μm. The bone volume to total tissue volume ratio (BV/TV, %) and trabecular separation (Tb.Sp, μm) were analyzed. These results were analyzed by Data Viewer and CTVox softwares.

Statistical Analysis. Each experiment was repeated at least 3 times with duplication for each samples tested. Statistical analysis was conducted using SPSS version 23.0. All the variables were expressed as the mean ± standard deviation (SD). Multiple comparisons among groups were evaluated by using a one-way ANOVA test. P values < 0.05 were considered to be statistically significant.

RESULTS

Identification of MSCs. MSCs exhibited whirl-like growth and displayed long spindle-shaped and fibroblast-like structures (Figure 1A,B). After chondrogenesis induction, Alcian blue

https://doi.org/10.1021/acsomega.4c11505
ACS Omega 2025, 10, 10633−10641

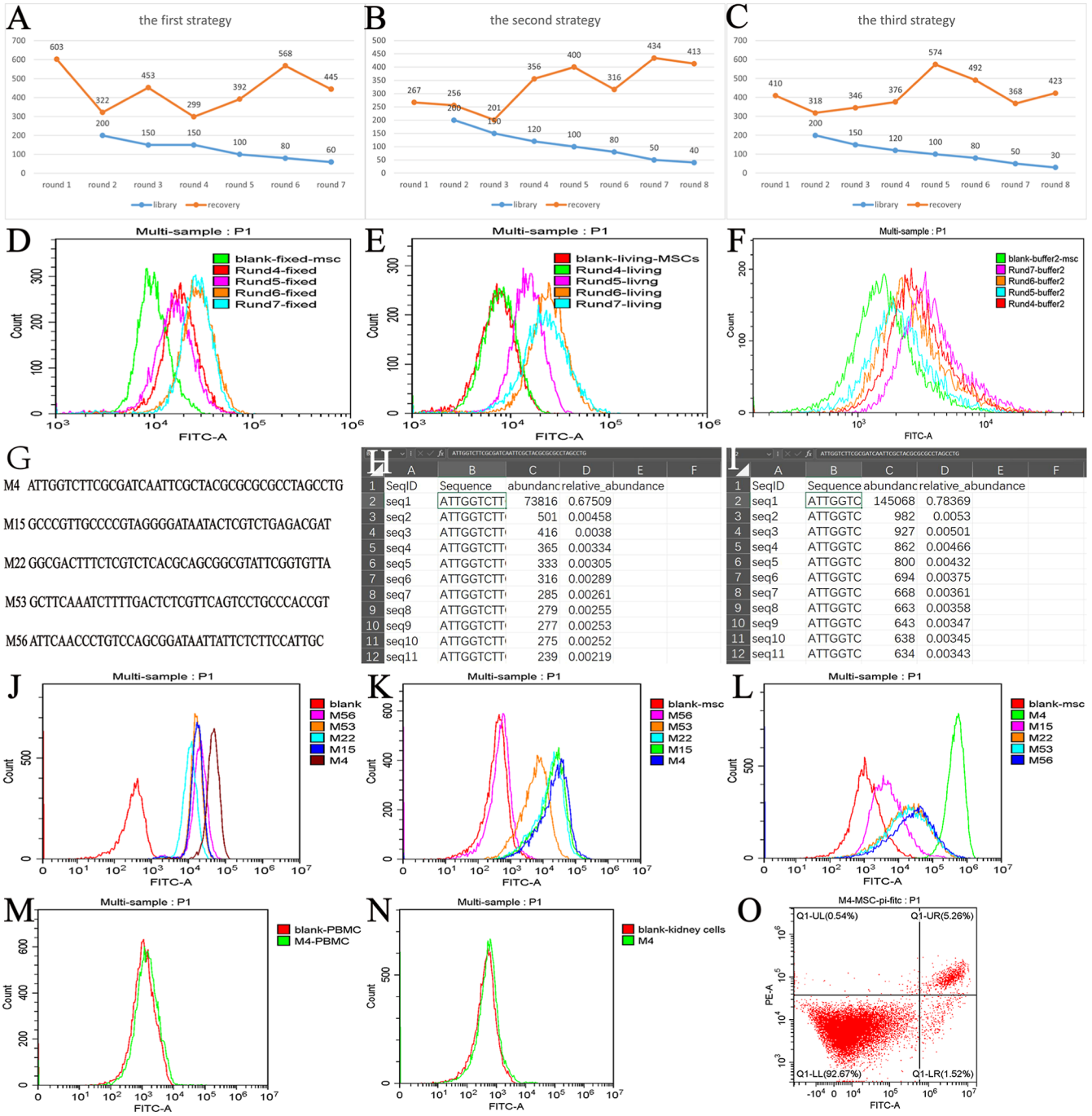

Figure 2. Cell-SELEX for the identification of MSC-specific aptamers. (A−C) The output-to-input ratio was recorded. (D−F) Libraries' enrichment of these three strategies was detected by flow cytometry. (G−I) Monoclonal sequencing and high-throughput sequencing were used to detect the ssDNA pools. (J−L) Flow cytometry to determine the binding affinity of the aptamer candidates (M4, M15, M22, M53, and M56) for MSCs. (M,N) Binding ability of M4 to nontarget cells (PBMC and kidney cells) as determined by flow cytometry. (O) Cytotoxicity of aptamer M4 to MSCs. From left to right: First strategy, second strategy, and third strategy.

staining showed acid mucopolysaccharides (Figure 1C). Flow cytometry suggested that MSCs were positive for CD29 and CD44 but negative for CD45 (Figure 1D−F).

Selection of MSC-Specific Aptamers. To monitor the enrichment process, we recorded the output-to-input ratio. The results showed that the output-to-input ratio gradually increased with the progression of SELEX, which indicated enrichment of the aptamer libraries (Figure 2A−C). We therefore used flow cytometry to detect enrichment libraries. The results suggested that the first, second, and third strategies had the highest fluorescence intensity in rounds sixth, sixth, and seventh, respectively (Figure 2D−F).

We sequenced the highly enriched ssDNA pool (sixth) from the first strategy and obtained fifty-seven sequences by monoclonal sequencing. The fifty-seven sequences were divided into six families on the basis of their homology and secondary structure analyzed using MEME and RNA structure softwares. Then, nine representative sequences were selected and compared to the two high-throughput results. Significantly, aptamer M4 accounted for the greatest proportion (67.5% and

https://doi.org/10.1021/acsomega.4c11505
ACS Omega 2025, 10, 10633−10641

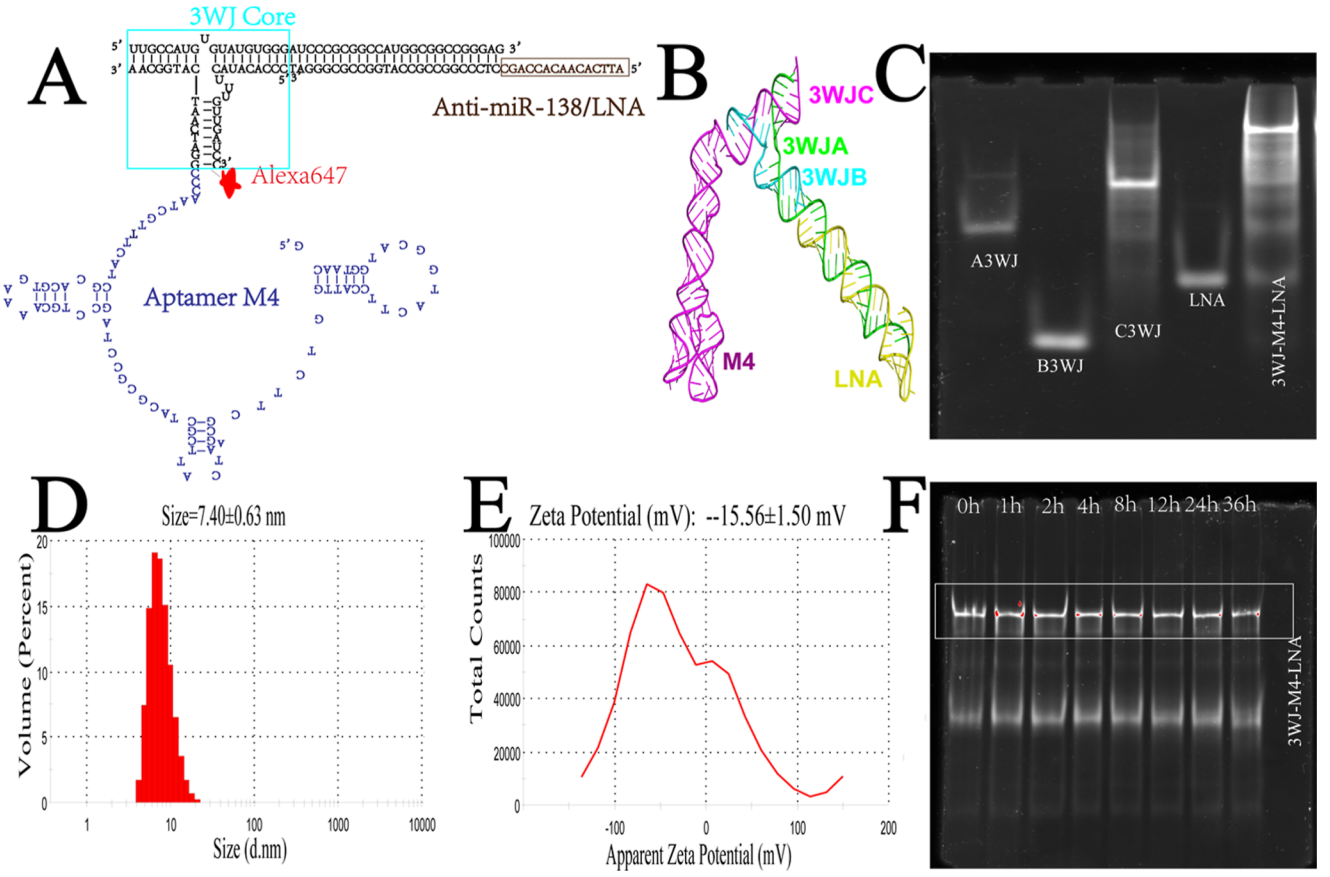

Figure 3. Construction and characteristics of 3WJ-M4-LNA nanoparticles. (A) 2D sequence of the nanoparticles. (B) 3D structures of 3WJ-M4-LNA nanoparticles. (C) Native PAGE gels showed highly efficient assembly of the nanoparticles. (D,E) Dynamic light scattering measurements were employed to analyze the hydrodynamic size and zeta potential. (F) Serum stability assay.

78.3%, respectively) of the total sequences (Figure 2G−I). To determine whether aptamer M4 has the highest affinity, four representative sequences (M15, M22, M53, and M56) that coexisted in the three results were selected for further investigation.

The results of flow cytometry showed that five sequences had good binding ability to MSCs in screening buffer I and screening buffer II (Figure 2J−L), but M4 had the highest affinity. What is more, flow cytometry analysis revealed that M4 bound with high affinity to MSCs but not rabbit PBMC and kidney cells (Figure 2M,N). Cytotoxicity tests revealed that the proportion of viable MSCs was 92.67% after incubation with aptamer M4 (Figure 2O). This result suggested that aptamer M4 was nearly nontoxic to MSCs.

Construction and Characteristics of 3WJ-M4-LNA Nanoparticles. The 3WJ derived from phi29 pRNA was used as the core scaffold to carry different modules: therapeutic agent LNA, aptamer M4, and fluorescent agent Alexa 647 (Figure 3A). The 3D structures of 3WJ-M4-LNA nanoparticles were analyzed through AlphaFold3 server (Figure 3B). The nanoparticles can assemble with high efficiency by mixing the four strands at an equal molar ratio in PBS buffer (Figure 3C). Dynamic light scattering showed that the size of the 3WJ-M4-LNA nanoparticles was 7.40 ± 0.63 nm (Figure 3D). And, the zeta potential of the nanoparticles was −15.56 ± 1.50 mV (Figure 3E), which indicated that the nanoparticles were highly negatively charged and did not aggregate in solution.

2′-F-modified U and C nucleotides were employed to strengthen the 3WJ-M4-LNA nanoparticles' serum stability. The results suggested that the nanoparticles remained with good stability within 36 h (Figure 3F). These results meant that the 3WJ-M4-LNA nanoparticles can be efficiently constructed as well as can be resistant to nucleases.

Binding and Internalization of 3WJ-M4-LNA Nanoparticles into MSCs. Confocal microscopy showed that the 3WJ-M4-LNA nanoparticles, but not 3WJ-LNA, can bind and be internalized into MSCs. As we can see in the picture, there was an excellent overlap of the red nanoparticles and green cytoplasm (Figure 4C). And, very low signal overlap was observed for blank and 3WJ-LNA groups (Figure 4A,B). Flow cytometry results also demonstrated that a stronger fluorescence signal was recorded in MSCs treated with 3WJ-M4-LNA nanoparticles (Figure 4D).

Western blot was employed to detect the osteogenic differentiation of MSCs after being treated by 3WJ-M4-LNA nanoparticles. First, we examined the miRNA-138 gene knockdown efficiency by the 3WJ-M4-LNA nanoparticles from 20 to 200 nM. The results of qPCR analysis revealed that the intracellular miR-138 amount was decreased to about 40% at 200 nM (Figure 4I, $P < 0.05$). Next, we examined the effects of 3WJ-M4-LNA nanoparticles on the osteogenic related proteins in MSCs. Using western blot analysis, we found the expression levels of Runx2 and OPN in the 3WJ-M4-LNA nanoparticle group are obviously higher than 3WJ-M4 and 3WJ-LNA groups (Figure 4J, $P < 0.05$). What is more, to understand the molecular mechanisms of 3WJ-M4-LNA nanoparticles, the activity of the ERK1/2 signaling was detected by western blot. The results showed that the

https://doi.org/10.1021/acsomega.4c11505
ACS Omega 2025, 10, 10633−10641

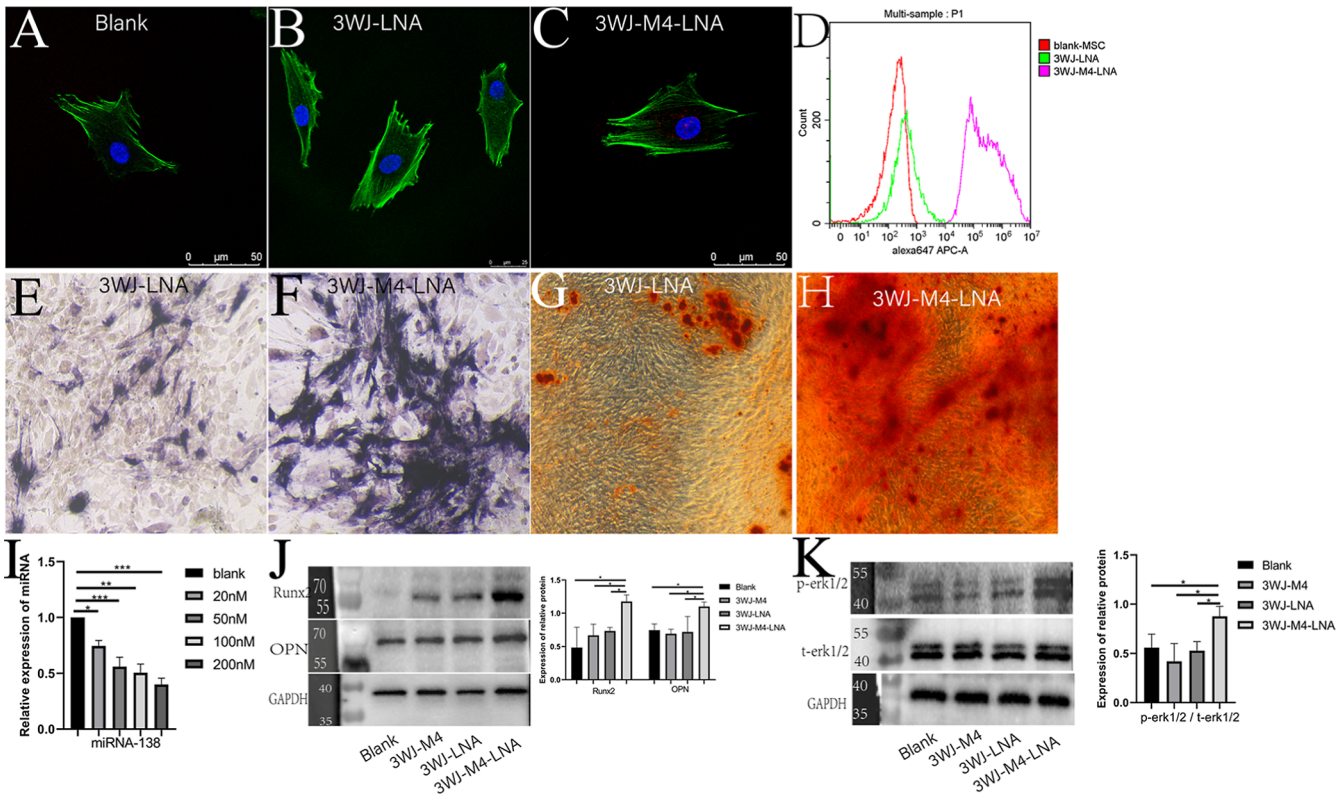

Figure 4. 3WJ-M4-LNA nanoparticles can bind to MSCs and promote the osteogenic differentiation of MSCs in vitro. (A−C) Confocal microscopy analysis of 3WJ-M4-LNA-Alexa 647 binding and entering MSCs. Cells incubated with 3WJ-LNA served as controls. Cytoskeleton was stained with Alexa Fluor 488 and nucleus was stained with DAPI. (D) Flow cytometry analysis was used to detect the binding between 3WJ-M4-LNA-Alexa 647 or 3WJ-LNA-Alexa 647 and MSCs. (E−H) ALP and alizarin red staining after being incubated with the 3WJ-M4-LNA nanoparticles. (I) qPCR analysis was employed to detect the gene knockdown efficiency of miRNA-138 in MSCs with different concentrations of 3WJ-M4-LNA. (J) Western blot was used to detect the expression of osteogenic related proteins in MSCs. (K) Western blot was used to detect the expression of *t*-erk1/2 and *p*-erk1/2 in MSCs. Data represent mean ± SD. $^{*}P < 0.05$, $^{**}P < 0.01$, and $^{***}P < 0.001$.

pERK1/2 protein level was increased in the 3WJ-M4-LNA nanoparticle group (Figure 4K, $P < 0.05$).

After 14 days of osteogenic induction, there was more obvious ALP and mineralized nodule production in MSCs treated with 3WJ-M4-LNA nanoparticles (Figure 4E−H). Thus, we have verified that the 3WJ-M4-LNA nanoparticles can be internalized into MSCs and enhance osteogenic potential of MSCs.

3WJ-M4-LNA Promoted Bone Repair In Vivo. The rabbit OP models were injected with 3WJ-M4-LNA-Alexa 647 for 12 h and then the rabbits were euthanized; organs and femurs were collected for tissue distribution analysis. The results showed that the nanoparticles specifically preserved in bone rather than other organs (Figure 5A). H&E staining was used to detect tissue inflammation and histopathological changes. The results showed that there was no apparent inflammatory infiltration in the organs (Figure 5B1−B4). These results showed that the nanoparticles have no significant toxic effect on important organs.

The CT images were used to evaluate bone mass and bone microarchitecture at 8 weeks. The results suggested that relative bone volume (BV/TV) and trabecular separation (Tb.Sp) were obviously improved when compared to the 3WJ-M4 group and 3WJ-LNA group ($P < 0.05$) (Figure 5C1−C4,D1,D2).

DISCUSSION

Many studies have demonstrated miRNA 138 as a negative regulator of bone formation.[34−36] In this study, we constructed 3WJ-M4-LNA nanoparticles that can directly target MSCs to deliver anti-miRNA 138.

The specific recognition ability is a precondition for the function of the 3WJ-M4-LNA nanoparticles. In this paper, a multistrategy SELEX method was designed according to the traditional cell-SELEX procedure. Generally, the SELEX procedure involves incubation, amplification, and partitioning. This process presents several challenges, including PCR amplification bias, ineffective partitioning, loss of sequences, changes or instability of targets, and even conformational changes.[37−40] And, the type of cell state and selection buffer were unitary. In fact, the affinity of aptamers can be obviously affected by different cell states and metal ions.[41] This multistrategy SELEX involves three types of cell states and binding buffers and does not suffer from cell states, selection solutions, nonspecific sequences, and accidental sequences. Eventually, we obtained aptamer M4 that was demonstrated to target MSCs but not PBMCs or kidney cells. And, the nanoparticles were mainly in bone while barely in heart, liver, spleen, lung, and kidney under the guidance of aptamer M4.

As nucleic acid drugs, short half-life that is caused by nucleases will make the application of the 3WJ nanoparticles limited. 2′-F and 2′-O methylation modifications are the two most common types of RNA modifications to construct

https://doi.org/10.1021/acsomega.4c11505
ACS Omega 2025, 10, 10633−10641

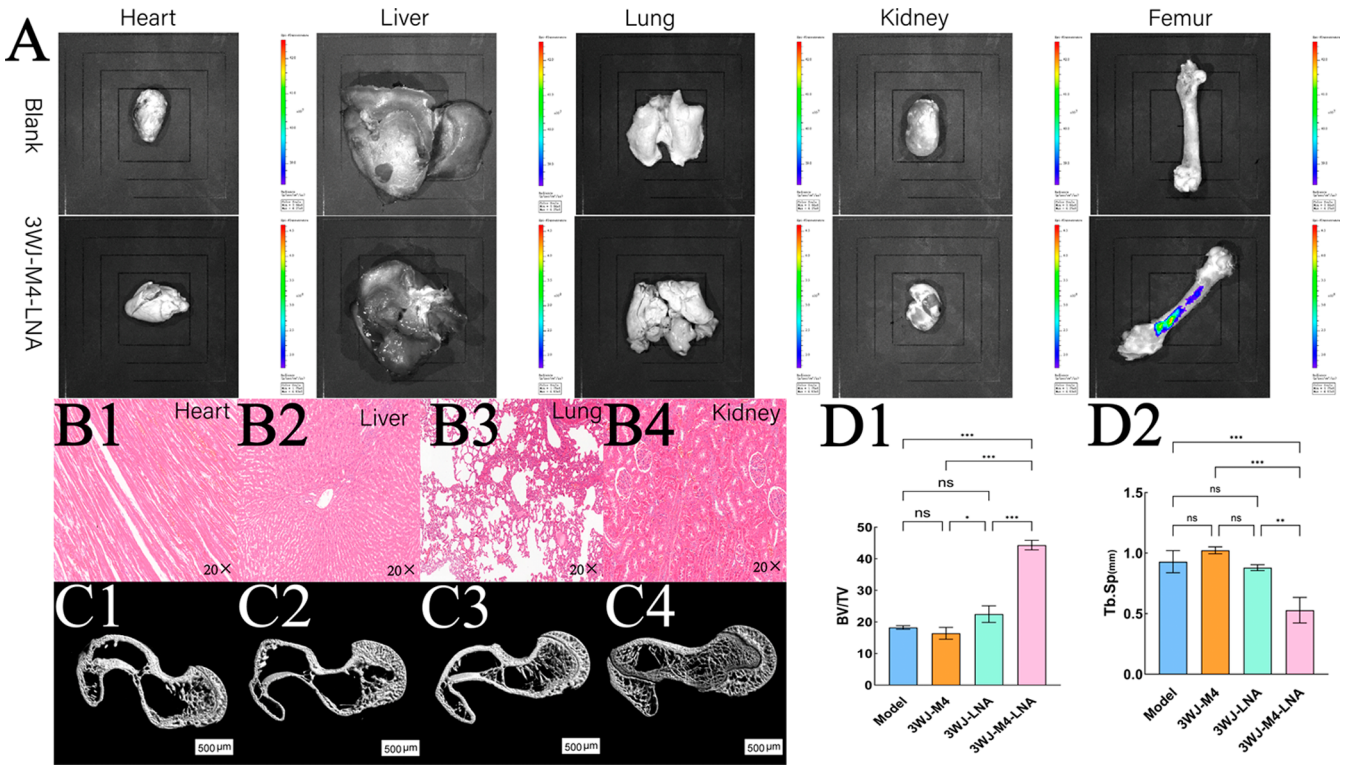

Figure 5. 3WJ-M4-LNA can promote bone formation. (A) Tissue distribution of 3WJ-M4-LNA in vivo. (B1−B4) Tissue inflammation and histopathological changes were detected by H&E staining. (C1−C4) Micro CT was used to recorded representative microarchitecture of the proximal femur in each group. From left to right: the model group, 3WJ-M4 group, 3WJ-LNA group, and 3WJ-M4-LNA group. (D1 and D2) Analysis of bone histomorphometric parameters (BV/TV and Tb.Sp) from rabbits in each group. Data represent mean ± SD. $^{*}P < 0.05$, $^{**}P < 0.01$, and $^{***}P < 0.001$.

RNase-resistant nanoparticles clinically and preclinically.[42−47] In this article, we employed 2′-F to modify the 3WJ nanoparticles. The results showed that the nanoparticles had good stability in 50% fetal bovine serum.

The effect of 3WJ nanoparticles on the expression of miRNA 138 was explored. First, confocal microscopy and flow cytometry images suggested efficient binding and internalization of the 3WJ nanoparticles into MSCs through aptamer M4-mediated endocytosis. We next detected the specific knockdown of miRNA 138 in MSCs through the 3WJ nanoparticles. We used LNA that has been reported to lead to affinity of anti-miRNAs to their complementary miRNAs to modify anti-miRNA 138.[48] Our results showed that the 3WJ nanoparticles can inhibit miRNA 138 expression in a dose-dependent manner. The results demonstrated that the 3WJ nanoparticles can effectively deliver anti-miRNA 138 LNA into MSCs based on specific binding of aptamer M4.

By exploring the effect of the 3WJ nanoparticles, we found that there was an obvious increase of the expression of osteogenic gene Runx2 and OPN. Runx2 is a key transcription factor and can promote MSCs' osteogenic differentiation by activating other osteogenic genes, such as BMP2, OPN, and many more.[49−52] We also explored the molecular mechanism of the 3WJ nanoparticles; we found that the phosphorylation of ERK1/2 was enhanced after miRNA 138 being inhibited. As a noncanonical signaling pathway, the ERK1/2 signaling pathway is involved in the proliferation, differentiation, and apoptosis of cells.[53,54] Many studies also have identified the ERK1/2 signaling pathway can regulate the osteogenic differentiation of MSCs and maintain bone homeostasis through promoting the activation of Runx2.[55−58] These results suggested that the 3WJ nanoparticles can promote MSCs' osteogenic differentiation through reducing the level of expression of miR-138 and activating the ERK1/2 pathway.

In summary, our current study successfully demonstrates the delivery of anti-miRNA 138 via the 3WJ nanoparticles as a therapeutic agent and provides a promising perspective for clinical applications to treat OP.

■ ASSOCIATED CONTENT

Data Availability Statement

The data is available throughout the manuscript and supporting files.

■ AUTHOR INFORMATION

Corresponding Author

Zhanghua Li − *Tongren Hospital Affiliated to Wuhan University, Wuhan, Hubei 430000, China;* orcid.org/0000-0002-9919-8111; Email: lizhanghua_123@163.com

Authors

Liangliang Xu − *Tongren Hospital Affiliated to Wuhan University, Wuhan, Hubei 430000, China*

Xiangzhong Liu − *Tongren Hospital Affiliated to Wuhan University, Wuhan, Hubei 430000, China*

Jian Chen − *Tongren Hospital Affiliated to Wuhan University, Wuhan, Hubei 430000, China; The First hospital of Nanchang, Nanchang, Jiangxi 330000, China*

Liwei Xu − *Wuhan Sports University, Wuhan 430079, China*

Aofei Yang − *Hubei Provincial Hospital of Traditional Chinese Medicine, Wuhan, Hubei 430000, China*

https://doi.org/10.1021/acsomega.4c11505
ACS Omega 2025, 10, 10633−10641

Complete contact information is available at:
https://pubs.acs.org/10.1021/acsomega.4c11505

Author Contributions

⊥LLX, XZL, and JC contributed equally to this work. ZHL designed experiments. LLX, XZL, and JC selected aptamer and constructed the 3WJ nanoparticles. LWX and AFY isolated and cultured MSCs, PBMCs, and kidney cells. The first draft was written by LLX, XZL, and JC. Then, was proofread by ZHL. All the authors have read and approved the final manuscript.

Funding

This work was supported by the National Natural Science Foundation of China [81472103], the Natural Science Fund of Hubei Province [2024AFB977], the Health Family Planning Research Fund of Wuhan City [WX18M01 and WZ22Q13], and Knowledge Innovation Special Project of Wuhan Municipal Bureau of Science and Technology [2022020801010547].

Funding

Animal experiments were approved by the Ethics Committee of Wuhan Third Hospital and followed the Guide for the Care and Use of Laboratory Animals. The approval number is SY2022−050.

Notes

The authors declare no competing financial interest.

REFERENCES

(1) Aibar-Almazán, A.; Voltes-Martínez, A.; Castellote-Caballero, Y.; Afanador-Restrepo, D. F.; Carcelén-Fraile, M. d. C.; López-Ruiz, E. Current Status of the Diagnosis and Management of Osteoporosis. *Int. J. Mol. Sci.* **2022**, *23* (16), 9465.

(2) Yu, B.; Wang, C. Y. Osteoporosis and periodontal diseases - An update on their association and mechanistic links. *Periodontol. 2000* **2022**, *89* (1), 99−113.

(3) Yu, W.; Xie, Z.; Li, J.; Lin, J.; Su, Z.; Che, Y.; Ye, F.; Zhang, Z.; Xu, P.; Zeng, Y.; Xu, X.; Li, Z.; Feng, P.; Mi, R.; Wu, Y.; Shen, H. Super enhancers targeting ZBTB16 in osteogenesis protect against osteoporosis. *Bone Res.* **2023**, *11* (1), 30.

(4) Guo, Y.; Ma, S.; Wang, D.; Mei, F.; Guo, Y.; Heng, B. C.; Zhang, S.; Huang, Y.; Wei, Y.; He, Y.; Liu, W.; Xu, M.; Zhang, X.; Chen, L.; Deng, X. HtrA3 paves the way for MSC migration and promotes osteogenesis. *Bioact. Mater.* **2024**, *38*, 399−410.

(5) Zhu, J.; Liu, Y.; Chen, C.; Chen, H.; Huang, J.; Luo, Y.; Zhao, K.; Chen, D.; Xu, Z.; Li, W.; Zhang, X.; Xiong, Y.; Xu, L.; Wang, B. Cyasterone accelerates fracture healing by promoting MSCs migration and osteogenesis. *J. Orthop. Translat.* **2021**, *28*, 28−38.

(6) Kilikevicius, A.; Meister, G.; Corey, D. R. Reexamining assumptions about miRNA-guided gene silencing. *Nucleic Acids Res.* **2022**, *50* (2), 617−634.

(7) Sumaiya, K.; Ponnusamy, T.; Natarajaseenivasan, K.; Shanmughapriya, S. Cardiac Metabolism and MiRNA Interference. *Int. J. Mol. Sci.* **2022**, *24* (1), 50.

(8) Diener, C.; Keller, A.; Meese, E. Emerging concepts of miRNA therapeutics: from cells to clinic. *Trends Genet.* **2022**, *38* (6), 613−626.

(9) Yang, Y.; Yujiao, W.; Fang, W.; Linhui, Y.; Ziqi, G.; Zhichen, W.; Zirui, W.; Shengwang, W. The roles of miRNA, lncRNA and circRNA in the development of osteoporosis. *Biol. Res.* **2020**, *53* (1), 40.

(10) Tsukamoto, S.; Løvendorf, M. B.; Park, J.; Salem, K. Z.; Reagan, M. R.; Manier, S.; Zavidij, O.; Rahmat, M.; Huynh, D.; Takagi, S.; Kawano, Y.; Kokubun, K.; Thrue, C. A.; Nagano, K.; Petri, A.; Roccaro, A. M.; Capelletti, M.; Baron, R.; Kauppinen, S.; Ghobrial, I. M. Inhibition of microRNA-138 enhances bone formation in multiple myeloma bone marrow niche. *Leukemia* **2018**, *32* (8), 1739−1750.

(11) Yan, J.; Chang, B.; Hu, X.; Cao, C.; Zhao, L.; Zhang, Y. Titanium implant functionalized with antimiR-138 delivered cell sheet for enhanced peri-implant bone formation and vascularization. *Mater. Sci. Eng., C* **2018**, *89*, 52−64.

(12) Ji, C.; Wei, J.; Zhang, L.; Hou, X.; Tan, J.; Yuan, Q.; Tan, W. Aptamer-Protein Interactions: From Regulation to Biomolecular Detection. *Chem. Rev.* **2023**, *123* (22), 12471−12506.

(13) Li, Y.; Tam, W. W.; Yu, Y.; Zhuo, Z.; Xue, Z.; Tsang, C.; Qiao, X.; Wang, X.; Wang, W.; Li, Y.; Tu, Y.; Gao, Y. The application of Aptamer in biomarker discovery. *Biomark. Res.* **2023**, *11* (1), 70.

(14) Brosseau, N. E.; Vallée, I.; Mayer-Scholl, A.; Ndao, M.; Karadjian, G. Aptamer-Based Technologies for Parasite Detection. *Sensors* **2023**, *23* (2), 562.

(15) Zhu, L.; Yuhan, J.; Yu, H.; Zhang, B.; Zhu, L.; He, X.; Huang, K.; Xu, W. Aptamer functionalized nucleic acid nano drug for targeted synergistic therapy for colon cancer. *J. Nanobiotechnol.* **2023**, *21* (1), 182.

(16) Liu, X.; Hu, J.; Ning, Y.; Xu, H.; Cai, H.; Yang, A.; Shi, Z.; Li, Z. Aptamer Technology and Its Applications in Bone Diseases. *Cell Transplant.* **2023**, *32*, 9636897221144949.

(17) Cesarini, V.; Scopa, C.; Silvestris, D. A.; Scafidi, A.; Petrera, V.; Del Baldo, G.; Gallo, A. Aptamer-Based In Vivo Therapeutic Targeting of Glioblastoma. *Molecules* **2020**, *25* (18), 4267.

(18) Xie, S.; Ai, L.; Cui, C.; Fu, T.; Cheng, X.; Qu, F.; Tan, W. Functional Aptamer-Embedded Nanomaterials for Diagnostics and Therapeutics. *ACS Appl. Mater. Interfaces* **2021**, *13* (8), 9542−9560.

(19) Wu, L.; Wang, Y.; Xu, X.; Liu, Y.; Lin, B.; Zhang, M.; Zhang, J.; Wan, S.; Yang, C.; Tan, W. Aptamer-Based Detection of Circulating Targets for Precision Medicine. *Chem. Rev.* **2021**, *121* (19), 12035−12105.

(20) Ren, Y.; Ge, K.; Tang, Q.; Liang, X.; Fan, L.; Ye, K.; Wang, M.; Yao, B. Dual-Recognition-Mediated Autocatalytic Amplification Assay for the Subpopulations of PD-L1 Positive Extracellular Vesicle. *Anal. Chem.* **2024**, *96*, 9585−9592.

(21) Chen, L.; Li, J. Mg2+ Ions Regulating 3WJ-PRNA to Construct Controllable RNA Nanoparticle Drug Delivery Platforms. *Pharmaceutics* **2022**, *14*, 1413.

(22) Shu, D.; Shu, Y.; Haque, F.; Abdelmawla, S.; Guo, P. Thermodynamically stable RNA three-way junction for constructing multifunctional nanoparticles for delivery of therapeutics. *Nat. Nanotechnol.* **2011**, *6* (10), 658−667.

(23) Pang, L.; Shah, H.; Wang, H.; Shu, D.; Qian, S. Y.; Sathish, V. EpCAM-Targeted 3WJ RNA Nanoparticle Harboring Delta-5-Desaturase siRNA Inhibited Lung Tumor Formation via DGLA Peroxidation. *Mol. Ther. Nucleic Acids* **2020**, *22*, 222−235.

(24) Yang, L.; Li, Z.; Binzel, D. W.; Guo, P.; Williams, T. M. Targeting oncogenic KRAS in non-small cell lung cancer with EGFR aptamer-conjugated multifunctional RNA nanoparticles. *Mol. Ther. Nucleic Acids* **2023**, *33*, 559−571.

(25) Liao, Y. C.; Cheng, T. C.; Tu, S. H.; Chang, J.; Guo, P.; Chen, L. C.; Ho, Y. S. Tumor targeting and therapeutic assessments of RNA nanoparticles carrying α9-nAChR aptamer and anti-miR-21 in triple-negative breast cancers. *Mol. Ther. Nucleic Acids* **2023**, *33*, 351−366.

(26) Sung, H.; Lloyd, T. E. Disrupted endoplasmic reticulum-mediated autophagosomal biogenesis in a Drosophila model of C9-ALS-FTD. *Autophagy* **2024**, *20*, 94−113.

(27) Khisamutdinov, E. F.; Bui, M. N.; Jasinski, D.; Zhao, Z.; Cui, Z.; Guo, P. Simple Method for Constructing RNA Triangle, Square, Pentagon by Tuning Interior RNA 3WJ Angle from 60° to 90° or 108°. *Methods Mol. Biol.* **2015**, *1316*, 181−193.

(28) Shu, D.; Khisamutdinov, E. F.; Zhang, L.; Guo, P. Programmable folding of fusion RNA in vivo and in vitro driven by pRNA 3WJ motif of phi29 DNA packaging motor. *Nucleic Acids Res.* **2014**, *42* (2), No. e10.

(29) Zhang, H.; Endrizzi, J. A.; Shu, Y.; Haque, F.; Sauter, C.; Shlyakhtenko, L. S.; Lyubchenko, Y.; Guo, P.; Chi, Y. I. Crystal structure of 3WJ core revealing divalent ion-promoted thermostability and assembly of the Phi29 hexameric motor pRNA. *RNA* **2013**, *19* (9), 1226−1237.

(30) Li, Z. H.; Liao, W.; Zhao, Q.; Huan, T.; Feng, P.; Wei, X.; Yi, Y.; Shao, N. S. Effect of Cbfa1 on osteogenic differentiation of mesenchymal stem cells under hypoxia condition. *Int. J. Clin. Exp. Med.* **2014**, *7* (3), 540−548.
(31) Binzel, D. W.; Khisamutdinov, E.; Vieweger, M.; Ortega, J.; Li, J.; Guo, P. Mechanism of three-component collision to produce ultrastable pRNA three-way junction of Phi29 DNA-packaging motor by kinetic assessment. *RNA* **2016**, *22*, 1710−1718.
(32) Jin, H.; Jiang, N.; Xu, W.; Zhang, Z.; Yang, Y.; Zhang, J.; Xu, H. Effect of flavonoids from Rhizoma Drynariae on osteoporosis rats and osteocytes. *Biomed. Pharmacother.* **2022**, *153*, 113379.
(33) Liang, C.; Guo, B.; Wu, H.; Shao, N.; Li, D.; Liu, J.; Dang, L.; Wang, C.; Li, H.; Li, S.; Lau, W. K.; Cao, Y.; Yang, Z.; Lu, C.; He, X.; Au, D. W.; Pan, X.; Zhang, B. T.; Lu, C.; Zhang, H.; Yue, K.; Qian, A.; Shang, P.; Xu, J.; Xiao, L.; Bian, Z.; Tan, W.; Liang, Z.; He, F.; Zhang, L.; Lu, A.; Zhang, G. Aptamer-functionalized lipid nanoparticles targeting osteoblasts as a novel RNA interference-based bone anabolic strategy. *Nat. Med.* **2015**, *21*, 288−294.
(34) Chen, Z.; Huai, Y.; Chen, G.; Liu, S.; Zhang, Y.; Li, D.; Zhao, F.; Chen, X.; Mao, W.; Wang, X.; Yin, C.; Yang, C.; Xu, X.; Ru, K.; Deng, X.; Hu, L.; Li, Y.; Peng, S.; Zhang, G.; Lin, X.; Qian, A. MiR-138−5p Targets MACF1 to Aggravate Aging-related Bone Loss. *Int. J. Biol. Sci.* **2022**, *18* (13), 4837−4852.
(35) Chen, Z.; Zhao, F.; Liang, C.; Hu, L.; Li, D.; Zhang, Y.; Yin, C.; Chen, L.; Wang, L.; Lin, X.; Su, P.; Ma, J.; Yang, C.; Tian, Y.; Zhang, W.; Li, Y.; Peng, S.; Chen, W.; Zhang, G.; Qian, A. Silencing of miR-138−5p sensitizes bone anabolic action to mechanical stimuli. *Theranostics* **2020**, *10* (26), 12263−12278.
(36) Brito, V. G. B.; Bell-Hensley, A.; McAlinden, A. MicroRNA-138: an emerging regulator of skeletal development, homeostasis, and disease. *Am. J. Physiol. Cell Physiol.* **2023**, *325* (6), C1387−C1400.
(37) Santarpia, G.; Carnes, E. Therapeutic Applications of Aptamers. *Int. J. Mol. Sci.* **2024**, *25*, 6742.
(38) Costanzo, H.; Gooch, J.; Tungsirisurp, S.; Frascione, N. The Development and Characterisation of ssDNA Aptamers via a Modified Cell-SELEX Methodology for the Detection of Human Red Blood Cells. *Int. J. Mol. Sci.* **2024**, *25*, 1814.
(39) Zhong, J.; Liu, D.; Yang, Q.; Ding, J.; Chen, X. A Novel DNA Aptamer Probe Recognizing Castration Resistant Prostate Cancer in vitro and in vivo Based on Cell-SELEX. *Drug Des., Dev. Ther.* **2024**, *18*, 859−870.
(40) Singh, N. K.; Wang, Y.; Wen, C.; Davis, B.; Wang, X.; Lee, K.; Wang, Y. High-affinity one-step aptamer selection using a non-fouling porous hydrogel. *Nat. Biotechnol.* **2024**, *42*, 1224−1231.
(41) Myres, G. J.; Kitt, J. P.; Harris, J. M. Raman Scattering Reveals Ion-Dependent G-Quadruplex Formation in the 15-mer Thrombin-Binding Aptamer upon Association with α-Thrombin. *Anal. Chem.* **2023**, *95* (44), 16160−16168.
(42) Shou, J.; Li, S.; Shi, W.; Zhang, S.; Zeng, Z.; Guo, Z.; Ye, Z.; Wen, Z.; Qiu, H.; Wang, J.; Zhou, M. 3WJ RNA Nanoparticles-Aptamer Functionalized Exosomes From M2Macrophages Target BMSCs to Promote the Healing of Bone Fractures. *Stem Cells Transl. Med.* **2023**, *12* (11), 758−774.
(43) Yang, L.; Li, Z.; Binzel, D. W.; Guo, P.; Williams, T. M. Targeting oncogenic KRAS in non-small cell lung cancer with EGFR aptamer-conjugated multifunctional RNA nanoparticles. *Mol. Ther. Nucleic Acids* **2023**, *33*, 559−571.
(44) Pang, H. H.; Huang, C. Y.; Chen, P. Y.; Li, N. S.; Hsu, Y. P.; Wu, J. K.; Fan, H. F.; Wei, K. C.; Yang, H. W. Bioengineered Bacteriophage-Like Nanoparticles as RNAi Therapeutics to Enhance Radiotherapy against Glioblastomas. *ACS Nano* **2023**, *17* (11), 10407−10422.
(45) Li, P.; Liu, Y.; Song, R.; Zhao, L.; Yang, J.; Lu, F.; Cao, X. RNA 2'-O-Methyltransferase Fibrillarin Facilitates Virus Entry Into Macrophages Through Inhibiting Type I Interferon Response. *Front. Immunol.* **2022**, *13*, 793582.
(46) Piao, X.; Wang, H.; Binzel, D. W.; Guo, P. Assessment and comparison of thermal stability of phosphorothioate-DNA, DNA, RNA, 2'-F RNA, and LNA in the context of Phi29 pRNA 3WJ. *RNA* **2018**, *24* (1), 67−76.
(47) Binzel, D. W.; Khisamutdinov, E. F.; Guo, P. Entropy-driven one-step formation of Phi29 pRNA 3WJ from three RNA fragments. *Biochemistry* **2014**, *53* (14), 2221−2231.
(48) Shu, D.; Li, H.; Shu, Y.; Xiong, G.; Carson, W.; Haque, F.; Xu, R.; Guo, P. Systemic Delivery of Anti-miRNA for Suppression of Triple Negative Breast Cancer Utilizing RNA Nanotechnology. *ACS Nano* **2015**, *9* (10), 9731−9740.
(49) Gargalionis, A. N.; Adamopoulos, C.; Vottis, C. T.; Papavassiliou, A. G.; Basdra, E. K. Runx2 and Polycystins in Bone Mechanotransduction: Challenges for Therapeutic Opportunities. *Int. J. Mol. Sci.* **2024**, *25* (10), 5291.
(50) Chen, X. J.; Shen, Y. S.; He, M. C.; Yang, F.; Yang, P.; Pang, F. X.; He, W.; Cao, Y. M.; Wei, Q. S. Polydatin promotes the osteogenic differentiation of human bone mesenchymal stem cells by activating the BMP2-Wnt/β-catenin signaling pathway. *Biomed. Pharmacother.* **2019**, *112*, 108746.
(51) Chen, J.; Yu, L.; Gao, T.; Dong, X.; Li, S.; Liu, Y.; Yang, J.; Xia, K.; Yu, Y.; Li, Y.; Wang, S.; Fan, Z.; Deng, H.; Guo, W. Nanofiber-induced hierarchically-porous magnesium phosphate bone cements accelerate bone regeneration by inhibiting Notch signaling. *Bioact. Mater.* **2024**, *37*, 459−476.
(52) Xu, H. J.; Liu, X. Z.; Yang, L.; Ning, Y.; Xu, L. L.; Sun, D. M.; Liao, W.; Yang, Y.; Li, Z. H. Runx2 overexpression promotes bone repair of osteonecrosis of the femoral head (ONFH). *Mol. Biol. Rep.* **2023**, *50* (6), 4769−4779.
(53) Zhang, M.; Hu, W.; Cai, C.; Wu, Y.; Li, J.; Dong, S. Advanced application of stimuli-responsive drug delivery system for inflammatory arthritis treatment. *Mater. Today Bio.* **2022**, *14*, 100223.
(54) Bianchi, E.; Rontauroli, S.; Tavernari, L.; Mirabile, M.; Pedrazzi, F.; Genovese, E.; Sartini, S.; Dall'Ora, M.; Grisendi, G.; Fabbiani, L.; Maccaferri, M.; Carretta, C.; Parenti, S.; Fantini, S.; Bartalucci, N.; Calabresi, L.; Balliu, M.; Guglielmelli, P.; Potenza, L.; Tagliafico, E.; Losi, L.; Dominici, M.; Luppi, M.; Vannucchi, A. M.; Manfredini, R. Inhibition of ERK1/2 signaling prevents bone marrow fibrosis by reducing osteopontin plasma levels in a myelofibrosis mouse model. *Leukemia* **2023**, *37* (5), 1068−1079.
(55) Park, K. R.; Lee, J. Y.; Cho, M.; Yun, H. M. Ziyuglycoside I Upregulates RUNX2 through ERK1/2 in Promoting Osteoblast Differentiation and Bone Mineralization. *Am. J. Chin Med.* **2021**, *49* (4), 883−900.
(56) Song, X.; Okabe, K.; Ohta, Y.; Ohara, G.; Toyama, N.; Chang, Q.; Wang, Y.; Hibi, H. Family with sequence similarity 20 member B regulates osteogenic differentiation of bone marrow mesenchymal stem cells on titanium surfaces. *Acta Biomater.* **2023**, *161*, 298−308.
(57) Valenti, M. T.; Dalle Carbonare, L.; Mottes, M. Ectopic expression of the osteogenic master gene RUNX2 in melanoma Maria Teresa Valenti, Luca Dalle Carbonare, Monica Mottes. *World J. Stem Cell.* **2018**, *10* (7), 78−81.
(58) Wang, J.; Fang, C. L.; Noller, K.; Wei, Z.; Liu, G.; Shen, K.; Song, K.; Cao, X.; Wan, M. Bone-derived PDGF-BB drives brain vascular calcification in male mice. *J. Clin. Invest.* **2023**, *133* (23), No. e168447.

https://doi.org/10.1021/acsomega.4c11505
ACS Omega 2025, 10, 10633−10641